

LRP 809/05

October 2005

**Electron heat transport in shaped TCV  
L-mode plasmas**

Y. Camenen, A. Pochelon, A. Bottino, S. Coda,  
F. Ryter, O. Sauter, R. Behn, T.P. Goodman,  
M.A. Henderson, A. Karpushov, L. Porte,  
G. Zhuang

accepted for publication in  
Plasma Phys. & Contr. Fusion

ISSN 0458-5895



# Electron heat transport in shaped TCV L-mode plasmas

Y Camenen<sup>1</sup>, A Pochelon<sup>1</sup>, A Bottino<sup>1</sup>, S Coda<sup>1</sup>, F Ryter<sup>2</sup>,  
O Sauter<sup>1</sup>, R Behn<sup>1</sup>, T P Goodman<sup>1</sup>, M A Henderson<sup>1</sup>,  
A Karpushov<sup>1</sup>, L Porte<sup>1</sup>, G Zhuang<sup>1</sup>

<sup>1</sup> Centre de Recherches en Physique des Plasmas, Association

EURATOM-Confédération Suisse, Ecole Polytechnique Fédérale de Lausanne (CRPP EPFL), CH-1015 Lausanne, Switzerland

<sup>2</sup> Max-Planck-Institut für Plasmaphysik, EURATOM-IPP Association, Garching, Germany

E-mail: [yann.camenen@epfl.ch](mailto:yann.camenen@epfl.ch)

**Abstract.** Electron heat transport experiments are performed in L-mode discharges at various plasma triangularities, using radially localized electron cyclotron heating to vary independently both the electron temperature  $T_e$  and the normalized electron temperature gradient  $R/L_{T_e}$  over a large range. Local gyro-fluid (GLF23) and global collisionless gyro-kinetic (LORB5) linear simulations show that, in the present experiments, trapped electron mode (TEM) is the most unstable mode. Experimentally, the electron heat diffusivity  $\chi_e$  is shown to decrease with increasing collisionality, and no dependence of  $\chi_e$  on  $R/L_{T_e}$  is observed at high  $R/L_{T_e}$  values. These two observations are consistent with the predictions of TEM simulations, which supports the fact that TEM plays a crucial role in electron heat transport. In addition, over the broad range of positive and negative triangularities investigated, the electron heat diffusivity is observed to decrease with decreasing plasma triangularity, leading to a strong increase of plasma confinement at negative triangularity.

PACS numbers: 52.55.Fa, 52.25.Fi, 52.35.Kt

## 1. Introduction

Improving the energy confinement is a way to increase the plasma temperature towards the conditions required for plasma ignition, while keeping the input power constant. As one of the primary factor degrading the energy confinement of tokamak plasmas is cross-field electron heat transport, one route to energy confinement improvement is a better understanding of electron heat transport. A small fraction of cross-field transport arises from Coulomb collisions and is described, in toroidal geometry, by the neoclassical theory. The main part, one or two orders of magnitude higher, is attributed to micro-turbulence, an active field of investigation where substantial progress has been achieved over recent years, in particular through the simulation of plasma micro-instabilities. The

experimental determination of the electron heat transport dependence on controllable plasma parameters can have several important consequences. First, it helps to improve plasma performance and to provide an easier access to low transport regimes such as the electron internal transport barrier (eITB) regime. Secondly, it allows for more accurate prediction of the energy confinement in future fusion devices, by providing experimental data to test the relevance of micro-instability simulations and/or to establish heuristic transport models.

The present study explores the experimental dependence of electron heat transport on electron temperature, electron temperature gradient, plasma shape and plasma collisionality in TCV. The electron temperature and electron temperature gradient are predicted to have a strong influence on the trapped electron mode (TEM) and electron temperature gradient mode (ETG) growth rates and have been shown experimentally to strongly modify the level of electron transport [1, 2]. Plasma shape is one of the fundamental parameters in a tokamak that strongly influence plasma properties and performance. Increasing the elongation allows higher plasma current at fixed magnetic field and also influences other operational limits such as the pressure [3, 4] and density limits [5]. Triangularity and elongation have a strong influence on the core stability, e.g. sawtooth stability [6], and on the edge plasma properties, in particular on the H-mode pedestal and ELM stability [7, 8]. Global confinement studies in Ohmic [9, 10] and in centrally EC heated L-mode plasmas [11, 12] showed the beneficial role of low or negative triangularity on the electron energy confinement time. On the contrary, similar studies in H-mode showed that, due to the contribution of the edge pedestal, the confinement time increases with plasma triangularity [7, 8]. The choice of L-mode plasmas for the study of electron heat transport minimizes the influence of the plasma edge stability on global confinement, allowing a more direct study of the genuine effect of plasma shape on core plasma confinement. Plasma collisionality has also been shown recently to play an essential role in particle transport [13, 14]. At low collisionality, central EC heating leads to a flattening of the density profile, whereas at high collisionality it leads to a peaking of the density profile [15]. This behavior has been attributed to a change of the dominant micro-instability, from the TEM mode at low collisionality to the ITG mode at high collisionality [13]. The stabilization of the TEM mode at high plasma collisionality is also expected to influence electron heat transport.

The specificity of the present study lies in the exploration of a large range of both electron temperature gradients and electron temperatures, allowing us to decouple the effects of these two quantities, and also in the investigation of the influence of plasma shaping, in particular the plasma triangularity, which is varied from negative to positive values.  $-0.4 < \delta < 0.4$ . This study is made possible by the unique properties of the TCV tokamak and its ECH system.

The rest of the paper is organized as follows. After a brief description of the TCV tokamak and auxiliary heating system, the experiments, as well as the diagnostics and methods used for their analysis, are presented in section 2. In section 3, the stability of trapped electron and ion temperature gradient modes in the present experiment is

discussed. The experimental dependence of electron heat transport on the electron temperature and electron temperature gradient is investigated in section 4, while section 5 and section 6 focus on the role of plasma shape and plasma collisionality, respectively. The conclusions are presented in section 7.

## 2. Electron temperature, electron temperature gradient and plasma triangularity variation

### 2.1. TCV description

The TCV tokamak (major radius  $R_0 = 0.88$  m, minor radius  $a \leq 0.25$  m, magnetic field  $B_T \leq 1.54$  T, plasma current  $I_p \leq 1$  MA) is designed to investigate the effects of plasma cross-section shaping. Plasma edge triangularity  $-0.7 \leq \delta \leq 1$  and plasma edge elongation  $0.9 \leq \kappa \leq 2.8$  have been achieved [16]. The auxiliary heating relies on electron cyclotron (EC) waves, usually polarized in X-mode, at the 2<sup>nd</sup> harmonic (X2) and 3<sup>rd</sup> harmonic (X3) frequencies, allowing the coupling of the power to any plasma shape. The X2 EC waves are produced at 82.7 GHz by six gyrotrons delivering a total nominal power of 3 MW coupled to the plasma from the low field side, using six independent launchers steerable during the discharge [17]. The X3 EC waves are produced at 118 GHz by three gyrotrons delivering a total nominal power of 1.5 MW coupled to the plasma from the top, using a single launcher that can also be steered during the discharge [18].

### 2.2. Plasma discharges and experimental conditions

Two sets of experiments have been performed to study the electron heat transport of L-mode plasmas in limiter configuration.

The "constant  $I_p$ " set of experiments is dedicated to the study of the electron heat transport dependence on the electron temperature  $T_e$  and on the normalized electron temperature gradient  $R/L_{T_e} = R\nabla T_e/T_e$ . The toroidal magnetic field  $B_T$ , the plasma elongation  $\kappa$  and the plasma current  $I_p$  are kept constant ( $B_T = 1.44$  T,  $\kappa = 1.6$  and  $I_p = 220$  kA), while two plasma triangularities are studied,  $\delta = 0.2$  and  $\delta = 0.4$ , with an edge safety factor  $q_{95}$  close to 5 (4.7 and 5.4, respectively). The temperature profile is modified by depositing 0.45 to 1.8 MW of radially localized X2 EC heating power at two different radial locations. The EC power is deposited off-axis at  $\rho_1 = 0.35$ , just outside the  $q = 1$  surface, or far off-axis, at  $\rho_2 = 0.7$ . Here, we define the normalized radius as  $\rho = \sqrt{V/V_{LCFS}}$ , where  $V$  and  $V_{LCFS}$  are the volumes delimited by the flux surface labelled by  $\rho$  and by the last closed flux surface, respectively. The sawtooth period response to the EC heating confirms that the EC power deposition at  $\rho_1$  takes place just outside the  $q = 1$  surface, as indicated by the increase of the sawtooth period (sawtooth stabilization), from 2 – 3 ms in Ohmic to above 10 ms with the total EC power, while increasing the power deposited at  $\rho_1$  [19].

The “constant  $q_{95}$ ” set of experiments focuses on the role of the plasma triangularity and special care is taken to achieve the same line averaged density, total power and EC power deposition radius in each plasma configuration. The toroidal magnetic field and the plasma elongation are kept constant ( $B_T = 1.44$  T,  $\kappa = 1.5$ ), with the plasma current varied such as to keep the edge safety factor constant,  $q_{95} = 3.5$ , while a large range of plasma triangularity, from negative to positive values, is explored,  $-0.4 < \delta < +0.4$ . In both the “constant  $I_p$ ” and “constant  $q_{95}$ ” sets, the density range is fixed to  $0.8 < \bar{n}_e < 1.8 \cdot 10^{19} \text{ m}^{-3}$ , such as to avoid excessive refraction of the EC beams ( $n_{e0}/n_{e\text{cut-off}} < 0.7$ ) while also ensuring full single pass absorption for the far off-axis deposition. The width of the EC beams, narrow compared to the plasma radius, allows for radially localized EC power deposition. The full width at half maximum of the EC power deposition  $\Delta\rho_{\text{EC}}$  never exceeds 0.1 of normalized radius and the power absorption is above 95%, as computed by the linear ray tracing code TORAY-GA [20]. A poloidal view of the plasma cross-section and of the EC beams is shown in figure 1, for simultaneous central and off-axis EC power deposition in a plasma with a triangularity  $\delta = 0.4$ .

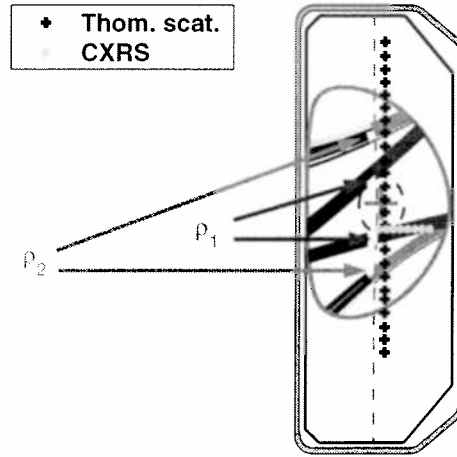


**Figure 1.** Poloidal view of the plasma cross section,  $\delta = 0.4$  and  $\kappa = 1.6$ , and of the EC beams for simultaneous EC power deposition at two radii,  $\rho_1$  and  $\rho_2$ . The cold resonance is indicated by the dashed line and the  $q=1$  surface by the dashed circle. The Thomson scattering and CXRS measurement location are indicated by crosses and dots, respectively.

### 2.3. Electron temperature profile and discharge response

The measurement of the electron density  $n_e$  and electron temperature  $T_e$  profiles, essential for this study, relies on Thomson scattering yielding coverage of the full plasma height with a spatial resolution of 4.5 cm, typically  $2 \times 8$  points in a profile, as shown in figure 1. The profiles are measured every 25 ms and averaged over  $\sim 300$  ms after stationary internal inductance  $l_i$  is reached. The temporal evolution of some plasma

parameters for a typical discharge of the "constant  $I_p$ " set of experiment is shown in figure 2 and the two phases used for the transport analysis are indicated. The EC mirror launchers were swept during the discharge to obtain different EC power deposition schemes in the two phases.

The normalized temperature and density gradients,  $R/L_{T_e}$  and  $R/L_{n_e}$ , are calculated

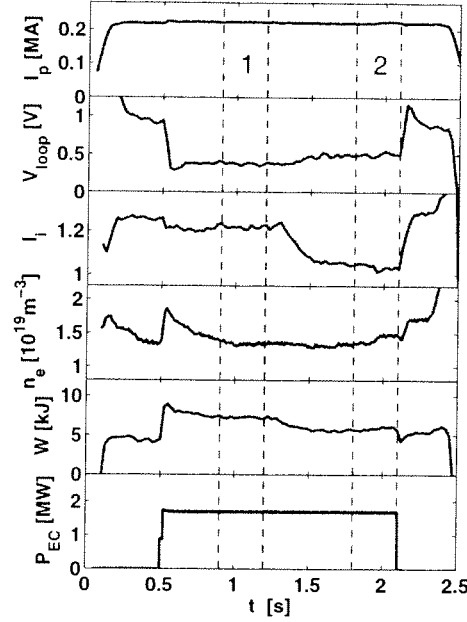


**Figure 2.** Temporal evolution of the plasma total current  $I_p$ , loop voltage  $V_{loop}$ , internal inductance  $l_i$ , electron density  $n_e$ , diamagnetic energy  $W$  and absorbed EC power  $P_{EC}$  for a typical discharge of the "constant  $I_p$ " set of experiment. The two phases delimited by the dashed lines are used for the transport analysis. In the first phase, the EC power deposition is 1.35 MW at  $\rho_1 = 0.35$  and 0.45 MW at  $\rho_2 = 0.7$ , whereas in the second phase it is 0.45 MW at  $\rho_1 = 0.35$  and 1.35 MW at  $\rho_2 = 0.7$ . The mirror launcher angles are changed between 1.25 and 1.4 s.

by mapping the temperature and density profiles on a real spatial coordinate chosen as the distance, measured at the outer mid-plane, from the torus axis to the considered flux surface.

Changing the amount of EC power deposited in the plasma and its spatial distribution allows for changing the electron temperature profile. Increasing the amount of EC power deposited at  $\rho_1$  only, from 0.45 to 1.8 MW, allows one to increase  $T_e$  without changing significantly the normalized temperature gradient:  $R/L_{T_e}$  only varies by 10% in the confinement region. This behavior, already observed in several tokamaks, is called profile stiffness [1]. In order to change the value of  $R/L_{T_e}$ , far off-axis distribution of a part or the totality of the EC power launched is needed, following the scheme developed in ASDEX Upgrade to study electron heat transport as a function of the normalized electron temperature gradient [21]. Far off-axis EC power deposition at  $\rho_2$  leads to low  $R/L_{T_e}$  values in the region of investigation,  $\rho_1 < \rho < \rho_2$ , whereas off-axis deposition at

$\rho_1$  leads to high  $R/L_{T_e}$  values. Intermediate  $R/L_{T_e}$  values are achieved by sharing the deposited EC power off-axis and far off-axis. In the "constant  $I_p$ " set of experiments, the variation of the total EC power and of the EC power distribution has allowed the achievement of strong variations of both  $T_e$  and  $R/L_{T_e}$  at mid-radius [22]. The variation of these two parameters at  $\rho = 0.53$  is shown in figure 3, together with data from ASDEX Upgrade for similar experiments. ASDEX Upgrade experiments are achieved in L-mode plasmas in divertor configuration, with a plasma elongation  $\kappa = 1.6$  and a plasma triangularity  $\delta = 0.25$ . The edge safety factor  $q_{95} = 4.5$  and the total EC power  $P_{EC} = 1.3$  MW are kept constant [21].

The flux surface averaged gradient of  $\rho$ ,  $\langle |\nabla\rho| \rangle$ , does not vary significantly with

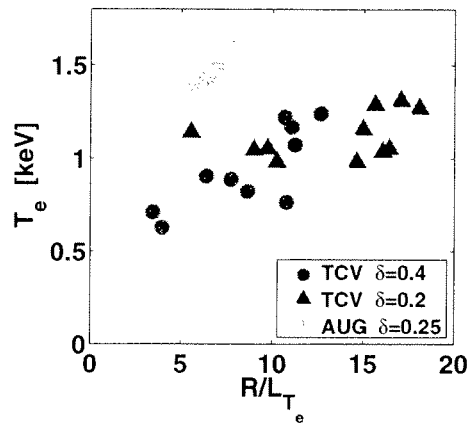


**Figure 3.** Range of electron temperature  $T_e$  and normalized temperature gradient  $R/L_{T_e}$  explored at  $\rho = 0.53$  in TCV and in similar ASDEX Upgrade electron heat transport experiments. In TCV,  $T_e$  and  $R/L_{T_e}$  are varied independently.

plasma triangularity (less than 5% at mid-radius). The higher  $R/L_{T_e}$  values obtained at  $\delta = 0.2$  as compared to  $\delta = 0.4$  are therefore not an artifact of the geometry due to the mapping of the  $T_e$  profile on a real space coordinate.

The relation between the electron temperature  $T_e$  and the electron heat flux  $Q_e$ , an indication of the level of cross-field electron heat transport, is obtained by calculating the electron thermal diffusivity  $\chi_e$  defined by

$$Q_e = -n_e \lambda_e \langle |\nabla\rho|^2 \rangle \frac{\partial T_e}{\partial \rho}$$

where the brackets indicate an average over the flux surface. As a linear relation between the electron heat flux  $Q_e$  and the electron temperature gradient  $\nabla T_e$  is assumed, the effect of off-diagonal terms in the transport matrix is not included. The electron heat flux is computed in steady-state taking into account the contributions of the Ohmic power, the EC power, and the power transferred from the electrons to the ions. A radially uniform loop voltage is assumed for the calculation of the Ohmic power, and the EC power deposition is obtained from the TORAY-GA ray tracing code. The ion



temperature profile, needed to estimate the power transfer from the electrons to the ions, is obtained from the Charge Exchange Recombination Spectroscopy diagnostic viewing the plasma region indicated in figure 1. The low plasma density results in a low equipartition power flow from the electrons to the ions and a high  $T_e/T_i$  ratio. The radiated power  $P_{\text{rad}}$  measured by XUV-bolometer photodiodes never exceeds 20% of the total power  $P_{\text{tot}}$ . Moreover, the ratio  $P_{\text{rad}}/P_{\text{tot}}$  remains below 5% for  $\rho < 0.8$  which therefore makes negligible the radiated power in the region of investigation  $\rho_1 < \rho < \rho_2$ . As shown in figure 4, the power balance is strongly dominated by the EC power. A

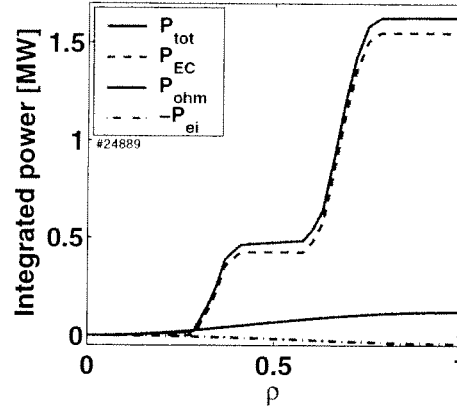


**Figure 4.** Power balance analysis showing the contributions of the EC power  $P_{\text{EC}}$ , the Ohmic power  $P_{\text{ohm}}$  and the equipartition power  $P_{\text{ei}}$  to the total power  $P_{\text{tot}}$ , for a case at  $\delta = 0.4$  with 0.45 MW of EC power deposited at  $\rho_1$  and 1.35 MW deposited at  $\rho_2$ .

change in the radial EC power distribution allows for a large variation of  $Q_e$  between  $\rho_1$  and  $\rho_2$  while keeping constant  $Q_e^{\text{edge}}$ . In the following, the local quantities are given at a normalized radius of  $\rho = 0.53$ , sufficiently far from the two EC power deposition radii,  $\rho_1$  and  $\rho_2$ , to avoid the large uncertainties on  $Q_e$  which could arise from the radial uncertainty of the EC power deposition calculations.

In the “constant  $I_p$ ” set of experiments, the EC waves are launched in the poloidal plane to achieve pure heating. The current drive component, due to the small angle with the magnetic field, represents less than 2% of the total plasma current, as evaluated using TORAY-GA. In the “constant  $q_{95}$ ” set of experiments, a small toroidal angle was added to the EC waves to reduce the current drive component to zero and by compensating for the inclination of the magnetic field lines. The plasma current density profile is calculated using the transport code PRETOR [23] in interpretative mode, consistently taking into account the experimental pressure profiles and the current density sources, Ohmic and bootstrap (EC driven current negligible), to reconstruct the magnetic equilibrium assuming steady-state conditions.

The neoclassical plasma resistivity depends on the plasma effective charge  $Z_{\text{eff}}$ , which is estimated from the experimental temperature and density profiles, loop voltage and

plasma current, assuming a flat  $Z_{\text{eff}}$  profile. The  $Z_{\text{eff}}$  value is estimated so as to match the value of the calculated total plasma current, taking into account the Ohmic and bootstrap contributions, with the value of the experimental one.

### 3. Micro-instability simulations

Let us first investigate the stability of electron temperature gradient (ETG), trapped electron (TEM) and ion temperature gradient (ITG) modes, which are potentially responsible for anomalous heat transport in the present plasma conditions. The temperature gradient threshold of the ETG instability derived from linear gyro-kinetic simulations [24] is found to be at least two times higher than the experimental values of  $R/L_{T_e}$  in the region  $0.2 < \rho < 0.7$ , due to the high  $Z_{\text{eff}}$  and  $T_e/T_i$  values. The ETG modes are therefore predicted to be stable in the region of investigation. On the other hand, local gyro-fluid linear simulations using GLF23 [25] indicate that TEM and ITG modes are unstable. The experimental values of the TEM mode driving terms  $R/L_{T_e}$  and  $R/L_{n_e}$ , at  $\rho = 0.53$ , are shown in figure 5. For most of the experimental

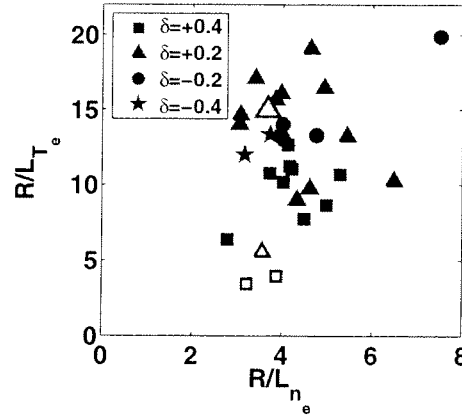


**Figure 5.** Experimental values of the driving gradients for TEM modes,  $R/L_{T_e}$  and  $R/L_{n_e}$ , at  $\rho = 0.53$ . From GLF23 simulations, the dominant instability exhibits a TEM mode behavior (full symbols), except for the lowest values of  $R/L_{T_e}$  (open symbols). The big symbol indicates a point also evaluated in LORB5 simulations.

conditions, the dominant instability exhibits a TEM mode behavior (full symbols in figure 5) in GLF23 simulations. First, the linear mode growth rate  $\gamma$  decreases strongly when  $R/L_{T_e}$  is reduced and increases when  $R/L_{T_i}$  is reduced. Secondly,  $\gamma$  is insensitive to  $T_e/T_i$  when  $T_e$  is kept constant, whereas  $\gamma$  strongly increases with  $T_e/T_i$  when  $T_i$  is kept constant. For the lowest  $R/L_{T_e}$  values, the dominant instability exhibits an ITG mode behavior (empty symbols in figure 5). In particular,  $\gamma$  increases strongly with  $R/L_{T_i}$  and is nearly insensitive to  $R/L_{T_e}$ .

Global collisionless gyro-kinetic simulations have been performed with the linear code LORB5 [26] for the experimental case indicated in figure 5. The mode growth rate

$\gamma = \gamma_{p,i} + \gamma_{d,i} + \gamma_{d,e}$  is calculated for toroidal mode numbers  $n$  ranging from 10 to 25. The quantities  $\gamma_{p,i}$ ,  $\gamma_{d,i}$  and  $\gamma_{d,e}$  indicate respectively the contribution of the ion parallel velocity, the ion drift velocity and the electron drift velocity terms to the total mode growth rate. The contribution of the electron channel is found to be more than 90% for all toroidal mode numbers (maximum growth rate obtained for  $n = 25$ ). The mode frequency indicates a TEM mode nature and the electrostatic potential fluctuations are localized between  $\rho = 0.4$  and  $\rho = 0.8$ .

Gyro-fluid and gyro-kinetic simulations show that in these experiments the stability of the TEM mode should play a crucial role in the transport of electron heat. For the present experiment, the variation of relevant parameters for the stability of ITG/TEM modes are given in table 1 at the investigation radius location ( $\rho = 0.53$ ). As in [27] we define an effective collisionality  $\nu_{\text{eff}} = \nu_{ei}/\omega_{De} \approx 0.1R\frac{n_e Z_{\text{eff}}}{T_e^2}$ , relevant to study the impact of collisions on electron heat transport (attributed to TEM and ITG modes) as it normalizes the collision frequency  $\nu_{ei}$  to the electron curvature drift frequency  $\omega_{De}$ , a rough estimate of the mode growth rate.  $f_t$  is the trapped particle fraction [28]. The safety factor and magnetic shear are evaluated using PRETOR.

**Table 1.** Range of parameters, relevant for the stability of ITG/TEM modes, explored in the present experiments ( $\rho = 0.53$ ).

$T_e$ [keV]	$T_i$ [keV]	$T_e/T_i$	$R/L_{T_e}$	$R/L_{T_i}$	$R/L_{n_e}$
0.6-1.3	0.2-0.5	2-4	4-20	3.5-6.5	3-7.5
$f_t$	$n_{e19}Z_{\text{eff}} [10^{19}\text{m}^{-3}]$	$\nu_{\text{eff}}$	$q$	$s$	
0.54-0.55	3.4-11.5	0.25-1	1.5-2	1-2	

#### 4. Experimental heat diffusivity dependence on $T_e$ and $R/L_{T_e}$

##### 4.1. Experimental observations

To investigate the effect of temperature  $T_e$  and normalized temperature gradient  $R/L_{T_e}$  on electron heat transport, we first concentrate on the plasma configuration of the "constant  $I_p$ " set of experiments with triangularity  $\delta = 0.4$ . In the experiment, the values of  $T_e$  and  $R/L_{T_e}$  are varied over a large range at mid-radius ( $T_e = 0.6\text{--}1.3\text{ keV}$  and  $R/L_{T_e} = 3.4\text{--}12.6$ ), while the values of  $n_e Z_{\text{eff}}$  and  $T_i$  remain roughly constant ( $n_e Z_{\text{eff}} = 3.5\text{--}4.5 \times 10^{19}\text{ m}^{-3}$  and  $T_i = 0.20\text{--}0.25\text{ keV}$ ). By changing both the total deposited EC power and the EC power distribution, the correlation between  $T_e$  and  $R/L_{T_e}$  is reduced: a variation of  $T_e$  by a factor of 1.7 at mid-radius is obtained at constant  $R/L_{T_e}$ , for the four discharges with  $R/L_{T_e} \sim 10.5$  shown in figure 3. The corresponding temperature profiles are shown in figure 6. The heat diffusivity  $\chi_e$ , calculated at  $\rho = 0.53$ , exhibits a strong dependence on  $T_e$ , as shown in figure 7, with little scatter despite the large variations of  $R/L_{T_e}$  and  $R/L_{n_e}$ . In comparison, the dependence of  $\chi_e$

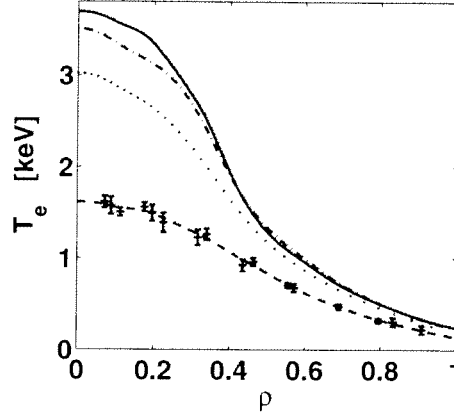


**Figure 6.** Temperature profiles from Thomson scattering for the four discharges with similar  $R/L_{T_e}$  value at mid-radius,  $R/L_{T_e} \sim 10.5$ , shown in figure 3. Error bars are shown for one profile as an example.

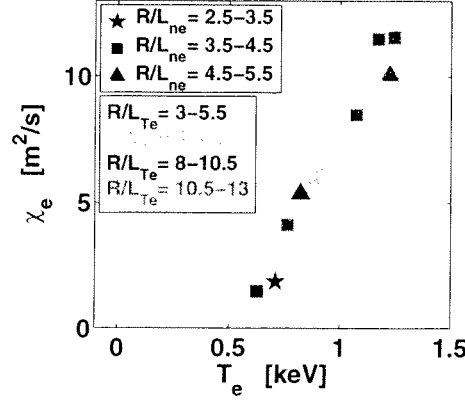


**Figure 7.** Strong dependence of the experimental electron heat diffusivity  $\chi_e$ , at mid-radius, on the electron temperature  $T_e$ . The ranges of  $R/L_{n_e}$  and  $R/L_{T_e}$  values are indicated by symbols and colors, respectively.

on  $R/L_{T_e}$  or  $R/L_{n_e}$ , shown in figure 8, is much weaker and the trend of  $\chi_e$  to increase with  $R/L_{T_e}$  can be attributed to the residual correlation of  $T_e$  and  $R/L_{T_e}$  visible in figure 3. The experimental observation of a strong dependence of  $\chi_e$  on  $T_e$  does not exclude the existence of a possible dependence on  $R/L_{T_e}$  or  $R/L_{n_e}$ , but this dependence has to be rather weak. This is in contrast with GLF23 linear simulations, where a clear and strong  $\chi_e$  dependence on both  $R/L_{T_e}$  and  $R/L_{n_e}$  is found, as shown in figure 9. This discrepancy is not understood at present. Note however that recent simulations estimating the TEM quasi-linear heat flux with the gyro-kinetic code GS2 predict that  $\chi_e$  no longer depends on  $R/L_{T_e}$  for high  $R/L_{T_e}$  values [29], in agreement with the present experiments.

Here, we must stress that in the present stationary experiments, the variation of the

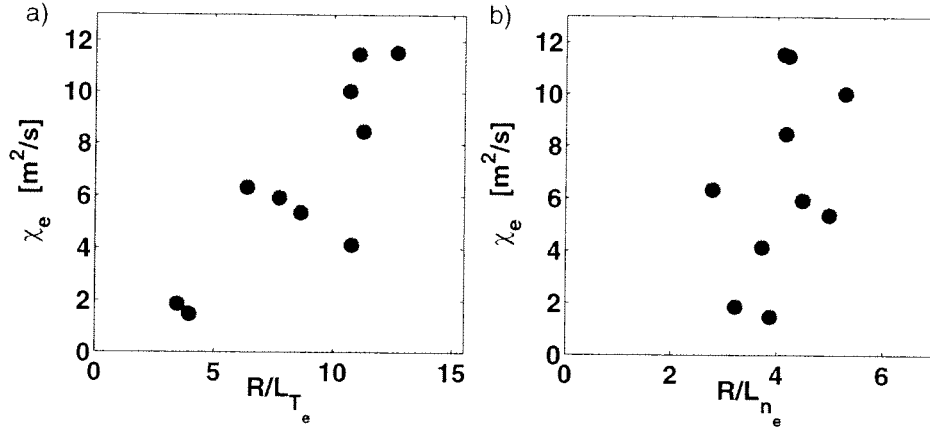


**Figure 8.** Experimental electron heat diffusivity  $\chi_e$ , at mid-radius, as a function of  
a)  $R/L_{T_e}$  (the four points at  $R/L_{T_e} \sim 10.5$  correspond to the four red squares in figure 7),  
b)  $R/L_{n_e}$ .

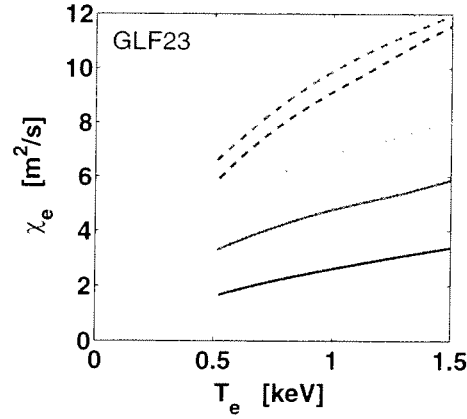


**Figure 9.** GLF23 simulation of the electron heat diffusivity  $\chi_e$ , at mid-radius, as a function of  $T_e$ , for various  $R/L_{T_e}$  and  $R/L_{n_e}$  values:  $R/L_{T_e} = 6$  (blue),  $R/L_{T_e} = 10$  (red),  $R/L_{T_e} = 14$  (green),  $R/L_{n_e} = 3$  (—),  $R/L_{n_e} = 5$  (- - -). The following quantities are kept constant:  $T_i = 0.2$  keV,  $n_e = 1.25 \times 10^{19} \text{ m}^{-3}$ ,  $Z_{\text{eff}} = 3$  (#24890,  $\delta = 0.4$ ).

temperature profile leads to a change of the current profile. The magnetic shear at mid-radius  $s$  increases with  $T_e$  from 1.1 to 1.6, which is expected to increase the electron heat transport. Recent experiments in TCV show that  $\chi_e$  is approximately proportional to  $s$  for  $s > 0$  [30]. Therefore, in the present experiments, the contribution of the shear variation to the variation of  $\chi_e$  would not exceed 5% of the total increase of  $\chi_e$ .

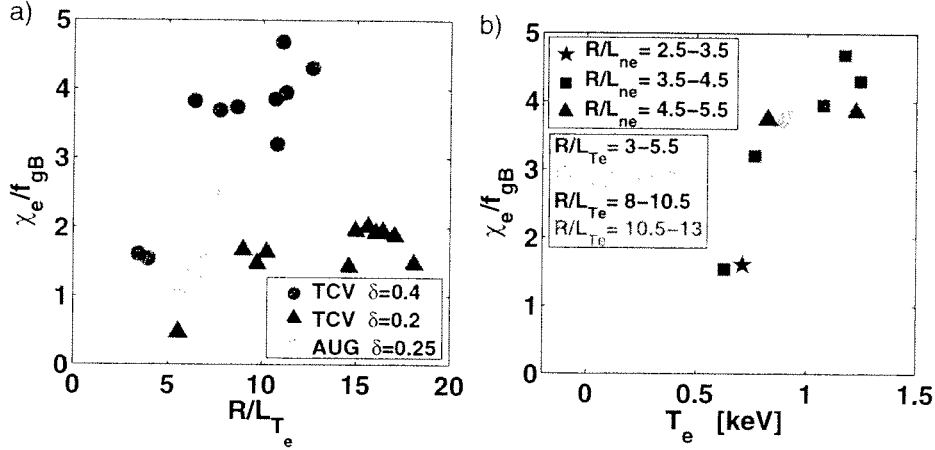


**Figure 10.** Electron heat diffusivity normalized to a gyro-Bohm scaling, as a function of

a)  $R/L_{T_e}$ , for TCV and ASDEX Upgrade data,

b)  $T_e$ , for TCV data at  $\delta = 0.4$ . The ranges of  $R/L_{n_e}$  and  $R/L_{T_e}$  values are indicated by symbols and colors, respectively. Similar results are obtained for  $\delta = 0.2$ .

#### 4.2. Gyro-Bohm normalization

A dependence of the electron heat diffusivity on the electron temperature is predicted by the gyro-Bohm scaling:

$$\chi_e^{gB} \propto \frac{T_e^{3/2}}{aB^2}$$

where  $a$  and  $B$  are the plasma minor radius and magnetic field, respectively. Such a dependence for the electron heat diffusivity is used in the heuristic critical gradient model described in [31, 32]. In this model, the electron heat diffusivity is proportional to  $f_{gB} = \frac{T_e^{3/2}}{aB^2}$  and  $q^{3/2}$ . A critical temperature gradient threshold  $R/L_{T_e}^{\text{crit}}$  is also introduced. For values of  $R/L_{T_e}$  below the threshold,  $\chi_e$  is constant, whereas for values of  $R/L_{T_e}$  above the threshold,  $\chi_e$  scales with  $R/L_{T_e} - R/L_{T_e}^{\text{crit}}$ . To test the experimental  $\chi_e$  dependence on  $R/L_{T_e}$  once the gyro-Bohm scaling is taken into account, we plot  $\chi_e/f_{gB}$  as a function of  $R/L_{T_e}$  in figure 10a, for the two triangularities of the "constant  $I_p$ " set of TCV experiments. ASDEX Upgrade data are also included in the figure. We first observe that for  $R/L_{T_e} > 8$ , a domain only explored in TCV, no dependence of  $\chi_e/f_{gB}$  on  $R/L_{T_e}$  is observed. In ASDEX Upgrade, for  $R/L_{T_e} < 8$ ,  $\chi_e/f_{gB}$  increases offset linearly with  $R/L_{T_e}$ . In the same  $R/L_{T_e}$  domain,  $R/L_{T_e} < 8$ , the few points obtained in TCV do not contradict the dependence observed in ASDEX Upgrade and the values of  $\chi_e/f_{gB}$  are similar in the two tokamaks. In addition, we can observe from TCV data that the gyro-Bohm scaling does not account for the whole dependence of  $\chi_e$  on  $T_e$ . This is demonstrated by the four points at  $\delta = 0.4$  with  $R/L_{T_e} \sim 10.5$  which still exhibit significantly different  $\chi_e/f_{gB}$  values, and is more explicitly shown in figure 10b where  $\chi_e/f_{gB}$  increases with  $T_e$ . As the variations of  $q$  at mid-radius are small, normalizing  $\chi_e$

to  $f_{gB}q^{3/2}$  instead of  $f_{gB}$  does not modify the results mentioned above.

The experimental finding that  $\chi_e/f_{gB}$  does not depend on  $R/L_{Te}$  for high  $R/L_{Te}$  values shown in figure 10, supports the recent quasi-linear simulations of TEM modes [29]. In these simulations the electron heat flux is found proportional to  $R/L_{Te} - R/L_{Te}^{\text{crit}}$ , which leads to  $\chi_e/f_{gB} \propto 1 - \frac{R/L_{Te}^{\text{crit}}}{R/L_{Te}}$ , and is in agreement with the variation of  $\chi_e/f_{gB}$  with  $R/L_{Te}$  observed in TCV [22]. It suggests strongly to include a weaker dependence on  $R/L_{Te}$  in the heuristic critical gradient model:  $\chi_e \propto 1 - \frac{R/L_{Te}^{\text{crit}}}{R/L_{Te}}$  seems more adequate than  $\chi_e \propto R/L_{Te} - R/L_{Te}^{\text{crit}}$ .

The difference in the level of transport observed in TCV plasmas with different triangularities,  $\delta = 0.2$  and  $\delta = 0.4$  will be addressed in the next sections.

## 5. Plasma shape effect

### 5.1. Experimental results

To investigate the effect of plasma triangularity  $\delta$  on electron heat transport, we compare two plasmas from the "constant  $q_{95}$ " set of experiments, with negative and positive triangularities,  $\delta = -0.4$  and  $\delta = +0.4$ , keeping constant other controlled plasma parameters in the two plasma configurations. The line averaged density measured on a central chord of the far infra-red interferometer is maintained constant,  $\bar{n}_e = 1.4 \cdot 10^{19} \text{ m}^{-3}$ , as are the total deposited EC power,  $P_{\text{EC}} = 1.3 \text{ MW}$  and the edge safety factor,  $q_{95} = 3.5$ . The edge safety factor is maintained constant by adjusting the total plasma current:  $I_p = 265 \text{ kA}$  at  $\delta = -0.4$  and  $I_p = 295 \text{ kA}$  at  $\delta = +0.4$ . As the EC power strongly dominates the power balance, the variation of the ohmic power due to the change in plasma current does not change significantly the electron edge heat flux. A clear reduction of electron heat transport is observed towards negative triangularities, resulting in substantially higher electron temperature, and lower electron heat diffusivity, at  $\delta = -0.4$  as compared to  $\delta = +0.4$ , see figure 11. In the two cases, the electron density and safety factor profiles are similar. The electron heat flux profiles are also similar, except for  $\rho < 0.45$  due to a slightly more off-axis EC power deposition at  $\delta = -0.4$  as compared to  $\delta = +0.4$ . The ion temperature follows the same trend than the electron temperature and is higher at  $\delta = -0.4$  than at  $\delta = +0.4$ . To evaluate the impact of the small variations of  $Q_e$ ,  $n_e$ , and  $\langle |\nabla \rho|^2 \rangle$  on the variation of  $\chi_e$  with  $\delta$ , we calculate:

- Profile 1:  $\chi_e$  at  $\delta = -0.4$
- Profile 2:  $\chi_e$  using as inputs the values of  $Q_e$ ,  $n_e$ ,  $\langle |\nabla \rho|^2 \rangle$  at  $\delta = +0.4$  and the value of  $\frac{\partial T_e}{\partial \rho}$  at  $\delta = -0.4$
- Profile 3:  $\chi_e$  using as inputs the values of  $Q_e$ ,  $n_e$ ,  $\langle |\nabla \rho|^2 \rangle$  at  $\delta = -0.4$  and the value of  $\frac{\partial T_e}{\partial \rho}$  at  $\delta = +0.4$
- Profile 4:  $\chi_e$  at  $\delta = +0.4$

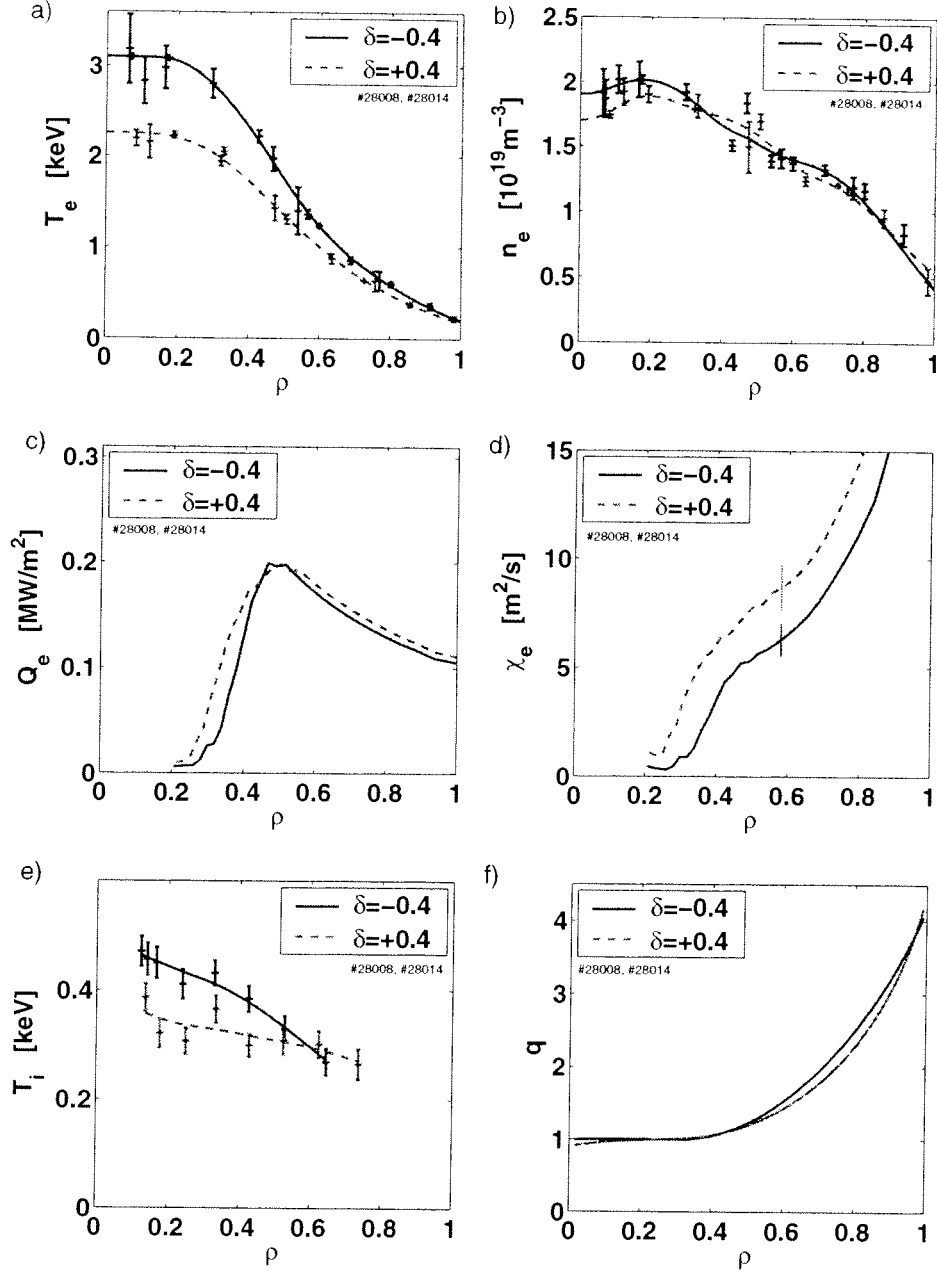


**Figure 11.** Electron temperature (a) increase obtained experimentally by reducing the plasma triangularity from  $\delta = +0.4$  (---) to  $\delta = -0.4$  (—), with similar electron density profile (b), and maintaining the edge safety factor and the electron heat flux (c) constant. The electron heat diffusivity (d) decreases with the plasma triangularity (error bars indicated at  $\rho = 0.58$ ). The ion temperature (e) is increased by the plasma triangularity reduction, while the safety factor profile (f) remains quite similar.

The resulting heat diffusivity profiles are plotted in figure 12. It appears clearly that for large radii,  $\rho > 0.45$ , the variation of  $\chi_e$  with plasma shape is not due to the



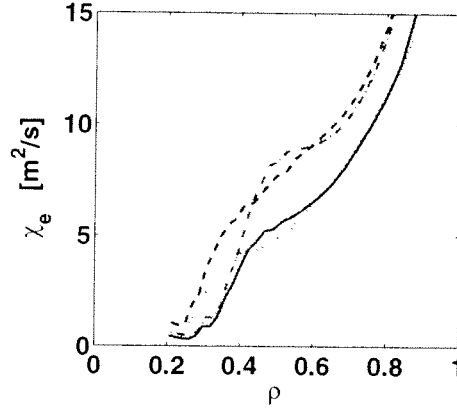


**Figure 12.** Power balance electron heat diffusivity profile:

- 1: (—) calculated at  $\delta = -0.4$ ,
- 2: (·····) calculated with the values of  $Q_e$ ,  $n_e$ ,  $\langle |\nabla\rho|^2 \rangle$  at  $\delta = +0.4$  and the value of  $\frac{\partial T_e}{\partial \rho}$  at  $\delta = -0.4$ ,
- 3: (— · —) calculated with the values of  $Q_e$ ,  $n_e$ ,  $\langle |\nabla\rho|^2 \rangle$  at  $\delta = -0.4$  and the value of  $\frac{\partial T_e}{\partial \rho}$  at  $\delta = +0.4$ ,
- 4: (- - -) calculated at  $\delta = +0.4$ .

small variations of  $Q_e$ ,  $n_e$ ,  $\langle |\nabla\rho|^2 \rangle$ : in this region, profile 2 is similar to profile 1, and profile 3 is similar to profile 4. For  $0.25 < \rho < 0.45$ , the higher heat diffusivity observed at  $\delta = +0.4$  compared to  $\delta = -0.4$  is due to a slightly more central EC power deposition, leading to a higher heat flux in this region, which tends to decrease the temperature variation with triangularity for  $\rho < 0.45$ . Therefore, the reduction of electron heat transport, observed for  $\rho > 0.45$  when decreasing the plasma triangularity from  $\delta = +0.4$  to  $\delta = -0.4$  is not due to a variation of the flux surfaces compression,  $Q_e$  or  $n_e$ , but should be attributed to the variation of plasma triangularity.

Reducing the triangularity from  $\delta = +0.4$  to  $\delta = -0.4$  in the experiment, the electron energy confinement time  $\tau_{Ee}$  increases from 3.6 to 5.3 ms and the electron energy confinement time normalized to the RLW model prediction [33] increases from 1.5 to 2.2. As a consequence, to obtain the same temperature profile, only half of the EC power used at a triangularity of  $\delta = +0.4$  ( $P_{EC} = 1.3$  MW) was required at  $\delta = -0.4$  ( $P_{EC} = 0.6$  MW), keeping constant the line averaged density and edge safety factor, see figure 13. The reduction of electron heat transport towards smaller plasma triangularity is significant and has a strong impact on the global plasma confinement.

## 5.2. Plasma shape variation in LORB5

To test the possible influence of plasma shape on ITG/TEM mode stability, simulations with the global linear collisionless gyro-kinetic code LORB5 [26] were performed. The code LORB5 is coupled with the CHEASE code, a Grad-Shafranov solver of tokamak

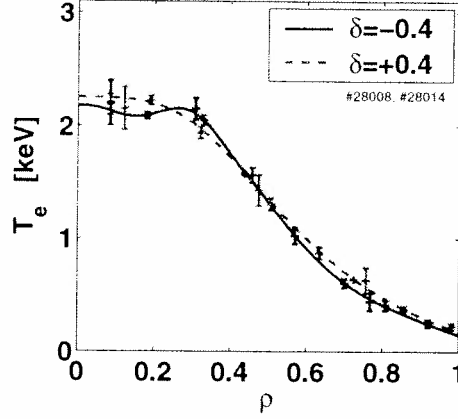


**Figure 13.** Quasi-identical  $T_e$  profile are obtained at  $\delta = -0.4$  (—) and  $\delta = +0.4$  (---) with only half of the EC power at  $\delta = -0.4$  as compared to  $\delta = +0.4$  (0.6 MW instead of 1.3 MW). The line averaged density and edge safety factor are kept constant.

plasma MHD equilibria [34]. The  $T_e$ ,  $T_i$  and  $n_e$  profiles used in the simulations are taken from the experimental  $\delta = 0.2$  equilibrium indicated in figure 5. The triangularity of the last closed flux surface is varied from -0.3 to 0.5 and the corresponding plasma equilibrium is reconstructed using CHEASE. As mentioned in section 3, the dominant instability in these conditions is a TEM mode. Moreover, the toroidal carbon ion velocity measured by the CXRS diagnostic is less than 10 km/s in the whole profile. The  $E \times B$  stabilization was therefore not included in the LORB5 simulation as it is expected to play an insignificant role. The calculated global mode growth rate and average radial extent do not depend significantly on the plasma triangularity, figure 14a, but the radial

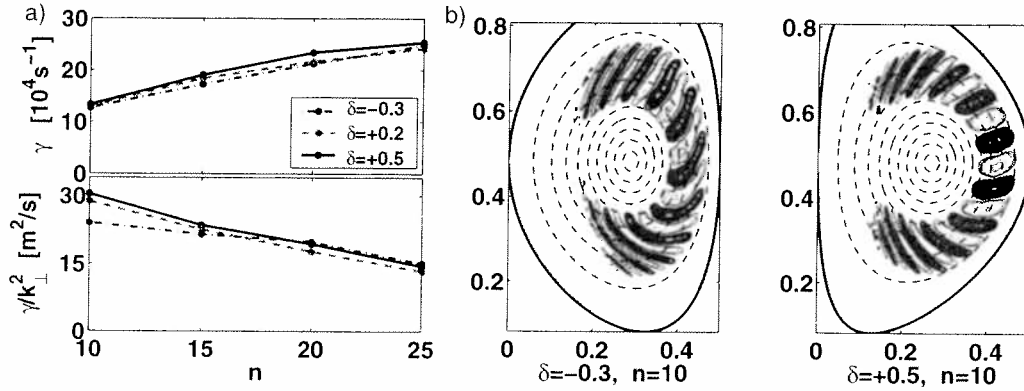


**Figure 14.** LORB5 simulations showing

a) the variation with the plasma triangularity of the mode growth rate  $\gamma$  and of the transport level estimated by a mixing length argument  $\gamma/k_{\perp}^2$ , for toroidal mode numbers ranging from 10 to 25.

b) the poloidal structure of the electrostatic potential at  $\delta = -0.3$  and  $\delta = +0.5$ , for toroidal mode number  $n = 10$ .

localization and structure of the electrostatic potential fluctuations,  $\tilde{\Phi}$ , changes with  $\delta$ , being displaced inwards toward negative triangularities, figure 14b. The change of the fluctuations localization and structure with  $\delta$  cannot easily be interpreted in terms of electron heat transport but underlines, together with the experimental observation of an increase of electron heat transport with  $\delta$ , that the full plasma geometry plays a role and should be taken into account in the simulation of ITG-TEM modes.

## 6. Separation of collisionality and shape effects

In TCV, the electron heat transport is observed to strongly decrease with increasing collisionality for the entire range of plasma triangularities explored, figure 15a and figure 15b. In figure 15a, the electron heat diffusivity calculated at  $\rho = 0.53$ , between the two EC power deposition radii, is plotted as a function of the effective collisionality  $\nu_{\text{eff}}$  for both triangularities,  $\delta = 0.2$  and  $\delta = 0.4$ , of the "constant  $I_p$ " set of experiments. The electron heat diffusivity  $\chi_e$  decreases with increasing  $\nu_{\text{eff}}$  and no dependence on the plasma triangularity is observed for this modest variation of triangularity. The value of  $n_e Z_{\text{eff}}$  at mid-radius is significantly higher at  $\delta = 0.2$  compared to  $\delta = 0.4$  and figure 15a suggests strongly that the  $\chi_e$  dependence on  $T_e$  discussed in section 4.1, observed at  $\delta = 0.4$  at constant  $n_e Z_{\text{eff}}$ , reflects primarily a dependence on  $\nu_{\text{eff}}$ . However it cannot be excluded that  $\chi_e$  could depend on both  $\nu_{\text{eff}}$  and  $T_e$  independently. The observation of a reduction of  $\chi_e$  with increasing  $\nu_{\text{eff}}$  in TCV is consistent with the expected stabilization of TEM modes at high collisionality, shown in GLF23 simulations, and with the reduction of electron heat transport with increasing  $\nu_{\text{eff}}$  observed in ASDEX Upgrade L-mode plasmas [35, 36]. In figure 15b,  $\chi_e$  is plotted as a function of the effective collisionality for the "constant  $q_{95}$ " set of experiments. Here also,  $\chi_e$  is observed to decrease with increasing  $\nu_{\text{eff}}$  and does not depend significantly on triangularity for positive  $\delta$  values. However, at negative triangularity,  $\chi_e$  clearly decreases with decreasing  $\delta$ , as was observed in section 5.1. In that set of experiments, the variation of  $I_p$  with  $\delta$ , imposed to maintain  $q_{95}$  constant, is parabolic with a minimum around  $\delta = -0.2$ . At constant  $\nu_{\text{eff}}$ , the monotonic reduction of  $\chi_e$  is therefore not due to the variation of  $I_p$  but indeed to the decrease of  $\delta$ . The coupled effect of  $\nu_{\text{eff}}$  and  $\delta$  allows us to understand why the reduction of  $\chi_e$  observed when reducing  $\delta$  from  $+0.4$  to  $-0.4$  is modest at constant heat flux, figure 11, while it has a strong impact on the required amount of EC power to achieve a given temperature, figure 13. At constant heat flux and plasma density, the reduction of  $\chi_e$  with decreasing  $\delta$  leads to an increase of  $T_e$ , and therefore to an increase of  $1/\nu_{\text{eff}}$ , which in turn leads to an increase of  $\chi_e$  and limits the increase of  $T_e$ . The strong reduction of  $\chi_e$  with  $\delta$  is thus partly masked by the increase of  $1/\nu_{\text{eff}}$ . On the other hand, if the effective collisionality is kept constant by adjusting the heat flux, the strong reduction of  $\chi_e$  with  $\delta$  is clearly shown by the reduction of the EC power required to match the electron temperatures at  $\delta = -0.4$  and at  $\delta = +0.4$ . To check whether the variation of  $\chi_e$  with  $\nu_{\text{eff}}$  is only due to a  $T_e^{3/2}$  gyro-Bohm dependence, we plot the gyro-Bohm normalized heat diffusivity  $\chi_e/f_{gB}$  as a function

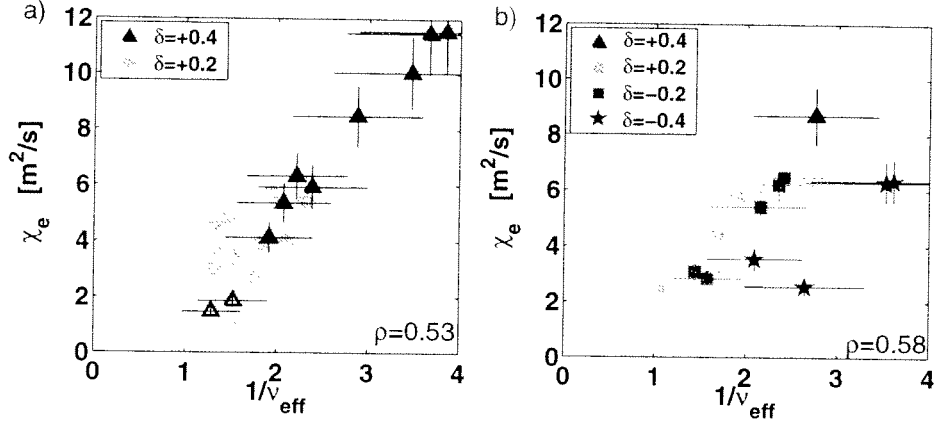


**Figure 15.** Experimental electron heat transport reduction at high plasma collisionality in

- a) the "constant  $I_p$ " set of experiments (open symbols indicates points where ITG mode dominates according to GLF23 simulations),
- b) the "constant  $q_{95}$ " set of experiments.

In the "constant  $q_{95}$ " set of experiments, a large range of plasma triangularity is explored and electron heat transport is observed to decrease at negative triangularity.

of  $1/\nu_{\text{eff}}$  in figure 16. It appears that an increase of the plasma collisionality and a decrease of the plasma triangularity still lead to a reduction of electron heat transport, even with a gyro-Bohm normalization. The  $\chi_e$  dependence on  $T_e^{3/2}$  of the gyro-Bohm scaling could be correct, but has to be completed with a  $\nu_{\text{eff}}$  and a  $\delta$  dependence. With or without gyro-Bohm normalization, the data show the significant effect of plasma collisionality and triangularity on the electron heat diffusivity  $\chi_e$ .

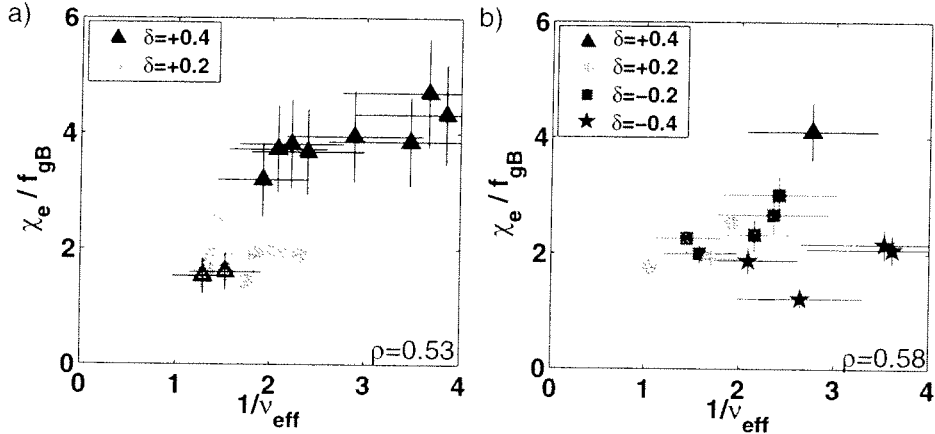


**Figure 16.** Experimental electron heat transport reduction at high plasma collisionality and negative plasma triangularity for the same data than in figure 15, but with a gyro-Bohm normalization for the electron heat diffusivity.

## 7. Conclusions

Core electron heat transport in low density L-mode plasmas has been investigated in TCV using strong localized EC heating to vary the electron temperature  $T_e$  and the normalized temperature gradient  $R/L_{T_e}$ . Both local linear gyro-fluid simulations (GLF23) and global collisionless gyro-kinetic simulations (LORB5) indicate that, in these experiments, TEM modes are unstable and should play a crucial role in the transport of electron heat. The experimental study was focused on the dependence of  $\chi_e$  on  $T_e$ ,  $R/L_{T_e}$  and  $\nu_{\text{eff}}$ , a set of plasma parameters predicted to have a strong influence on the TEM mode growth rate. In addition, the effect of plasma shape was investigated by varying the plasma triangularity  $\delta$  from negative to positive values. The study was performed in L-mode plasmas, since in H-mode the known pedestal height dependence on  $\delta$  affects the global energy confinement and makes the interpretation of the  $\delta$  effect on core electron heat transport more difficult. The  $\chi_e$  dependence observed in the present L-mode plasmas is expected to be a feature specific to TEM dominated transport.

The electron heat transport dependence on  $T_e$  and  $R/L_{T_e}$  has been tested experimentally by varying independently these two parameters over a range larger than earlier explored. The electron temperature was changed mainly by changing the total amount of EC power deposited in the discharge, while the temperature gradient was changed by changing the radial EC power distribution.

The experimental electron heat diffusivity, calculated at mid-radius, is found to strongly increase with the electron temperature with no strong dependence on  $R/L_{T_e}$  nor  $R/L_{n_e}$ . This result has been obtained at constant  $n_e Z_{\text{eff}}$ . The fact that  $\chi_e$  is experimentally shown not to depend on  $R/L_{T_e}$ , at high  $R/L_{T_e}$  values, specifies better the  $\chi_e$  dependence on  $R/L_{T_e}$  in the heuristic critical gradient model and supports recent quasi-linear simulations of TEM modes predicting that  $\chi_e \propto 1 - \frac{R/L_{T_e}^{\text{crit}}}{R/L_{T_e}}$ .

Comparing data with different values of  $n_e Z_{\text{eff}}$ , it appears that  $\chi_e$  not only depends on  $T_e$  but also on  $n_e Z_{\text{eff}}$  and that the electron heat diffusivity, as well as the electron heat diffusivity normalized to gyro-Bohm scaling, decreases strongly with increasing effective collisionality  $\nu_{\text{eff}} = 0.1 R \frac{n_e Z_{\text{eff}}}{T_e^2}$ . This experimental reduction of electron heat transport with  $\nu_{\text{eff}}$  is consistent with the predicted stabilizing effect of  $\nu_{\text{eff}}$  on the TEM modes and with the strong experimental impact of the effective collisionality on particle transport. The dependence of  $\chi_e$  on  $T_e$  and  $\nu_{\text{eff}}$  have not been separated, and it is not excluded that  $\chi_e$  could depend independently on  $T_e$  and  $\nu_{\text{eff}}$ .

These results suggest that the effective collisionality has to be included in the heuristic modelling of electron heat transport, together with a decrease of the impact of  $R/L_{T_e}$  on  $\chi_e$  at high  $R/L_{T_e}$  values.

The influence of plasma shape on local electron heat transport has also been addressed in these TEM modes dominated plasmas, by varying the plasma triangularity from positive to negative values. The experimental electron heat diffusivity decreases with the plasma triangularity and this decrease becomes stronger at very negative plasma triangularity.

As a consequence, the electron energy confinement time increases towards negative plasma triangularities, which drastically reduces the amount of EC power required at negative triangularity, as compared to positive triangularity, to obtain the same electron temperature profile. These experiments have allowed to separate the influence of plasma shape, here triangularity, and collisionality on electron heat transport.

## Acknowledgments

The authors would like to acknowledge fruitful discussions with C. Angioni and L. Villard.

Global simulations were performed on the parallel servers SGI Origin 3800 and the Linux cluster PLEIADES of the Ecole Polytechnique Fédérale de Lausanne.

## References

- [1] F. Ryter, C. Angioni, M. Beurskens, S. Cirant, G.T. Hoang, G.M.D. Hogeweij, F. Imbeaux, A. Jacchia, P. Mantica, W. Suttrop, and G. Tardini. *Plasma Phys. Control. Fusion*, 43:A323, 2001.
- [2] G.T. Hoang, C. Bourdelle, X. Garbet, G. Giruzzi, T. Aniel, and M. Ottaviani. *Phys. Rev. Lett.*, 87:125001, 2001.
- [3] F. Troyon, R. Gruber, H. Saurenmann, S. Semenzato, and S. Succi. *Plasma Phys. Control. Fusion*, 26:209, 1984.
- [4] F. Hofmann, O. Sauter, H. Reimerdes, I. Furno, and A. Pochelon. *Phys. Rev. Lett.*, 81:2918, 1998.
- [5] M. Greenwald, J.L. Terry, S.M. Wolfe, S. Ejima, M.G. Bell, S.M. Kaye, and G.H. Neilson. *Nucl. Fus.*, 28:2199, 1988.
- [6] H. Reimerdes, A. Pochelon, O. Sauter, T.P. Goodman, M.A. Henderson, and An. Martynov. *Plasma Phys. Control. Fusion*, 42:629, 2000.
- [7] J. Stober, O. Gruber, A. Kallenbach, V. Mertens, F. Ryter, A. Stabler, W. Suttrop, W. Treutterer, and the ASDEX Upgrade Team. *Plasma Phys. Control. Fusion*, 42:A211, 2000.
- [8] G. Saibene, R. Sartori, A. Loarte, D.J. Campbell, P.J. Lomas, V. Parail, K.D. Zastrow, Y. Andrew, S. Sharapov, A. Korotkov, M. Becoulet, G.T.A. Huysmans, H.R. Koslowski, R. Budny, G.D. Conway, J. Stober, W. Suttrop, A. Kallenbach, M. von Hellermann, and M. Beurskens. *Plasma Phys. Control. Fusion*, 44:1769, 2002.
- [9] J.-M. Moret, S. Franke, H. Weisen, M. Anton, R. Behn, B.P. Duval, F. Hofmann, B. Joye, Y. Martin, C. Nieswand, Z.A. Pietrzyk, and W. van Toledo. *Phys. Rev. Lett.*, 79:2057, 1997.
- [10] H. Weisen, J.-M. Moret, S. Franke, I. Furno, Y. Martin, M. Anton, R. Behn, M.J. Dutch, B.P. Duval, F. Hofmann, B. Joye, C. Nieswand, Z.A. Pietrzyk, and W. Van Toledo. *Nucl. Fus.*, 37:1741, 1997.
- [11] A. Pochelon, T.P. Goodman, and M.A. Henderson et al. *Nucl. Fus.*, 39:1807, 1999.
- [12] A. Pochelon et al. *Proc. 26th EPS Conference on Controlled Fusion and Plasma Physics (Maastricht, Netherlands)*, 23J:1089, 1999.
- [13] C. Angioni, A.G. Peeters, G.V. Pereverzev, F. Ryter, and G. Tardini. *Phys. Rev. Lett.*, 90:205003, 2003.
- [14] H. Weisen, A. Zabolotsky, C. Angioni, I. Furno, X. Garbet, C. Giroud, H. Leggate, P. Mantica, D. Mazon, J. Weiland, L. Zabeo, and K.-D. Zastrow. *Nucl. Fus.*, 45:L1, 2005.
- [15] C. Angioni, A.G. Peeters, X. Garbet, A. Manini, and F. Ryter. *Nucl. Fus.*, 44:827, 2004.
- [16] F. Hofmann et al. *Plasma Phys. Control. Fusion*, 43:A161, 2001.
- [17] T.P. Goodman, S. Alberti, M.A. Henderson, A. Pochelon, and M.Q. Tran. *Proc. 19th Symposium on Fusion Technology (Lisbon, Portugal)*, I:565, 1996.

- [18] J.-P. Hogge, S. Alberti, L. Porte, and G. Arnoux. *Nucl. Fus.*, 43:1353, 2003.
- [19] C. Angioni, T.P. Goodman, M.A. Henderson, and O. Sauter. *Nucl. Fus.*, 43:455, 2003.
- [20] K. Matsuda. *IEEE Trans. Plasma Sci.*, 17:6, 1989.
- [21] F. Ryter, G. Tardini, F. De Luca, H.-U. Fahrbach, F. Imbeaux, A. Jacchia, K.K. Kirov, F. Leuterer, P. Mantica, A.G. Peeters, G. Pereverzev, and W. Suttrop. *Nucl. Fus.*, 43:1396, 2003.
- [22] A. Pochelon, Y. Camenen, R. Behn, A. Bortolon, A. Bottino, S. Coda, B.P. Duval, E. Fable, T.P. Goodman, M.A. Henderson, A.N. Karpushov, J.-M. Moret, A. Mck, E. Nelson-Melby, L. Porte, F. Ryter, O. Sauter, A. Scarabosio, and G. Zhuang. *Proceedings of the 20th IAEA Fusion Energy Conference (Vilamoura, Portugal)*, IAEA-CN-116/EX/9-1.
- [23] D. Boucher and P.H. Rebut. *Proc. IAEA Tech. Committee Meeting on Advances in Simulation and Modelling of Thermonuclear Plasmas (Montreal, Canada)*, p.142.
- [24] F. Jenko, W. Dorland, and G.W. Hammett. *Phys. Plasmas*, 8:4096, 2001.
- [25] W. Dorland G. W. Hammett M. Kotschenreuther R. E. Waltz, G. M. Staebler and J. A. Konings. *Phys. Plasmas*, 4:2482, 1997.
- [26] A. Bottino, A.G. Peeters, O. Sauter, J. Vaclavik, and L. Villard. *Phys. Plasmas*, 11:198, 2004.
- [27] C. Angioni, A.G. Peeters, G.V. Pereverzev, F. Ryter, and G. Tardini. *Phys. Plasmas*, 10:3225, 2003.
- [28] Y.R. Lin-Liu and R.L. Miller. *Phys. Plasmas*, 2:1666, 1995.
- [29] A.G. Peeters, C. Angioni, M. Apostoliceanu, F. Jenko, and F. Ryter. *Phys. Plasmas*, 12:022505, 2005.
- [30] S. Cirant, S. Alberti, F. Gandini, R. Behn, and T.P. Goodman. *Proceedings of the 20th IAEA Fusion Energy Conference (Vilamoura, Portugal)*, IAEA-CN-116/EX/9-1.
- [31] F. Imbeaux, F. Ryter, and X. Garbet. *Plasma Phys. Control. Fusion*, 43:1503, 2001.
- [32] X. Garbet, P. Mantica, F. Ryter, G. Cordey, F. Imbeaux, C. Sozzi, A. Manini, E. Asp, V. Parail, and R. Wolf. *Plasma Phys. Control. Fusion*, 46:1351, 2004.
- [33] P.H. Rebut, P.P. Lallia, and M.L. Watkins. *Proceedings of the 12th International Conference on Plasma Physics and Controlled Nuclear Fusion Research. Nice 1988*, 2:1991, 1989.
- [34] H. Lütjens, A. Bondeson, and A. Roy. *Comput. Phys. Comm.*, 69:287, 1992.
- [35] C. Angioni, A.G. Peeters, F. Ryter, F. Jenko, G.D. Conway, T. Dannert, H.U. Fahrbach, M. Reich, and W. Suttrop. *Phys. Plasmas*, 12:040701, 2005.
- [36] F. Ryter, C. Angioni, A.G. Peeters, F. Leuterer, H.-U. Fahrbach, and W. Suttrop. *Phys. Rev. Lett.*, 95:085001, 2005.